AIMS Materials Science, 6(5): 713–729.
DOI: 10.3934/matersci.2019.5.713
Received: 21 May 2019
Accepted: 16 July 2019
Published: 09 August 2019

http://www.aimspress.com/journal/Materials

Research article

Surface modification of Ti6Al4V alloy for implants by anodization and electrodeposition

Jie Sun[1], Tzvetanka Boiadjieva-Scherzer[1,*], Hermann Kronberger[2], Kevin Staats[3], Johannes Holinka[3] and Reinhard Windhager[3]

[1] Centre of Electrochemical Surface Technology GmbH (CEST), Austria
[2] Technical University of Vienna, Institute of Chemical Technologies and Analytics, Austria
[3] Medical University of Vienna, Department of Orthopedics and Trauma Surgery, Austria

*** Correspondence:** Email: tzvetanka.boiadjieva@cest.at.

Abstract: Ti6Al4V alloy and Ti were subjected to anodization, aiming at a defined nano-topography as a basis for further surface modifications focused on enhancement of the antibacterial properties and biocompatibility of the material for implants. The anodization parameters (voltage and time), the electrolyte composition and acidity were varied in order to grow uniform phosphate-doped nano-tube-shaped structures with a diameter of 100 nm. Subsequently, Se and Se alloys (Ag_2Se and Cu_2Se) were uniformly incorporated into the titania nanotubes by pulse electrodeposition. Se-doped hydroxyapatite top coating was formed by precipitation. The electrochemical respond of modified Ti-based substrates and the electrodeposition process of Se and Se alloys were studied by cyclic voltammetry. Electrochemically and chemically treated surfaces were characterized by EDX, SEM, FIB, Raman spectroscopy and XRD. *In vitro* experiments with bacteria *Staphylococcus epidermidis* were conducted to evaluate the ability of the modified surfaces to prevent biofilm formation. Most promising results were obtained with Se–pTNT and Cu_2Se–pTNT.

Keywords: titania nanotube; selenium; copper selenide; silver selenide; hydroxyapatite

1. Introduction

Titanium metal and its alloys are the second most extensively used materials for fabricating implants in the biomedical sector after stainless steel [1]. Their suitability for the application arises from their favorable tensile strength, flexibility, corrosion resistance, high hemo- and

biocompatibility properties [2]. Despite their wide use, titanium-based implant materials suffer from the drawback of susceptibility to bacteria-induced inflammation, which causes loosening of the implants and other complications [3]. Antibiotic treatment of the inflammations is increasingly becoming ineffective due to development of drug resistant bacterial strains [4].

An alternative to antibiotics is the creation of a defined nano-topography on the surface of the implant materials, which inhibits adherence of bacterial cells to them. One of the methods used for surface nano-structuring of Ti-based materials is anodization in fluoride containing electrolytes, resulting in formation of nanotubes [5–9]. It has been shown that the presence of nanotubes of 100 nm diameter promotes osseointegration and antibacterial efficiency even without the use of pharmaceuticals [6,10,11]. In order to enhance the antibacterial properties, the nanotubes can be loaded with antibacterial agents like Ag [12], Cu [9], Se [13,14] and zinc selenide [15]. Se in particular exhibits osteogenic and antimicrobial activity, while suppressing inflammations. Studies with Se nanoparticles produced from precipitation indicate decrease in the function of adhesion-mediating proteins, inducing the production of damaging reactive oxygen species and inhibition of the proliferation of macrophages [14]. Se compounds like copper selenide [7] and silver selenide are attractive for implant surface modification due to low solubility, making it suited for low long-term release of antibacterial agents.

The biocompatibility and bioactivity of the implant material can be improved by an additional coating of a bone like substance of hydroxyapatite (HAp), a hydroxyl containing form of calcium phosphate, which promotes bone formation and growth [16]. Crystalline HAp provides mechanical stability, but has been shown to degrade slowly in simulated body fluid leading to insufficient bone ingrowth [17]. Amorphous HAp has a slightly higher solubility, which promotes faster initial bone fixation due to resorption and bioactivity [18].

In the present work, the three described approaches (Figure 1) for surface modification were combined to produce bacteria-resistant titanium-based implants for medical testing. The electrolyte composition and anodization parameters were varied in order to obtain nano-tube-shaped structures with a diameter of 100 nm on the surface of pure Ti and Ti6Al4V alloy substrates. The nanotubes were grown to contain phosphate for the promotion of osseointegration [19] and to be subsequently filled with antibacterial agents. Electrodeposition processes were used to deposit Se and Se alloys (Ag_2Se and Cu_2Se/Cu_3Se_2) on the nano-structured surfaces and monitored through CVA and constant voltage polarization techniques.

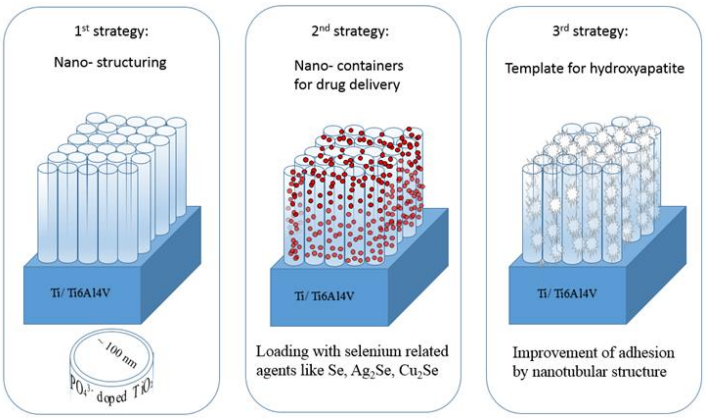

Figure 1. Schematic illustration of the three different strategies.

Electrochemically and chemically treated surfaces were characterized by EDX, SEM, FIB, RAMAN spectroscopy and XRD.

2. Materials and method

2.1. Nano-structuring of Ti and Ti6Al4V

Ti samples of 99.6% purity (Good Fellow, 10 mm × 5 mm, 2 mm thickness) and Ti6Al4V discs (10 mm diameter, 2 mm thickness) were grinded, polished, degreased with acetone and ethanol, and cathodically activated in 1 M H_2SO_4 for 10 min before anodization. For nanopattering, the anodization was performed in a two-electrode configuration with the specimen as anode positioned in 2 cm distance from the Pt foil (10 mm × 15 mm), which served as counter electrode. Ti and Ti6Al4V samples were anodically polarized in a fluoride containing solution at constant potentials.

Experiments were performed with pure Ti in order to gain a better understanding of the material's behavior during anodization without the interferences by alloying elements. The parameters were then applied on the alloy Ti6Al4V, which is one of the most common implant materials. Ti6Al4V behaves different during the anodization due to the presence of alpha (stabilized by Al) and beta phases (stabilized by V). During the anodization β-Ti grains are dissolved to a larger extend than those containing Al, resulting in gaps in the layer. This occurs because vanadium does not form oxides resistant to corrosion under these conditions. The reduction of available vanadium at the surface is a convenient side effect minimizing possible health risks from vanadium.

Aqueous phosphate and ethylene glycol-based electrolytes containing 0.12 M NH_4F were investigated in order to select the better suited for the substrate structuring (formation of uniform phosphate-doped nano-tubes with a diameter of 100 nm). Overview on the experiments is presented in Table 1.

Table 1. Experiment table.

Surface modifications	Constant parameters	Varied parameters		
Nanostructuring in an aqueous electrolyte	Ti/Ti6Al4V, 20 V	2 pH	3.3 pH	4.7 pH
	Ti/Ti6Al4V, pH 2	10 V	20 V	30 V
Nanostructuring in an ethylene based electrolyte	Ti/Ti6Al4V, 30 V	2 vol%	10 vol%	20 vol%
	Ti/Ti6Al4V, 10 vol% H_2O	20 V	30 V	40 V
Nanostructuring in an organic electrolyte with phosphate additive	Ti/Ti6Al4V, EG + 10 vol% H_2O, 30 V	10 mM	15 mM	
	Ti/Ti6Al4V, EG + 20 vol% H_2O, 30 V	10 mM	15 mM	
Electrodeposition of Se related coating	nanostructured Ti/Ti6Al4V substrate	Se	Ag_2Se	Cu_2Se
Influence of substrate's surface on the hydroxyapatite (HAp) deposition	50 ℃	Polished Ti	Unannealed pTNT from aqueous electrolyte (pH 2, 20 V)	Se–HAp on unannealed pTNT from ethylene glycol based electrolyte (EG, 10 vol% H_2O, 10 mM phosphate, 30 V)
	60 ℃	annealed pTNT from ethylene glycol electrolyte (EG, 10 vol% H_2O, 10 mM phosphate, 30 V)	Se-HAp on annealed pTNT from ethylene glycol (EG, 10 vol% H_2O, 10 mM phosphate, 30 V)	

The first samples series was anodized in an aqueous phosphate electrolyte containing 0.5 M phosphate, as either H_3PO_4 and/or $(NH_4)NaH(PO_4)\cdot 4H_2O$, pH value 2, 3.3 and 4.7 with voltages 10 V, 20 V and 30 V for 45 min. The second series was obtained by anodization for 1.5 h at voltages 20 V, 30 V and 40 V in an ethylene glycol based electrolyte containing 2 vol%, 10 vol% or 20 vol% deionized H_2O with/without 10 mM or 15 mM $(NH_4)NaH(PO_4)\cdot 4H_2O$. The as-prepared samples were cleaned by one-minute ultrasonication in ethylene glycol and subsequently annealed in air (450 ℃, 2 h) to transform TiO_2 phase(s) into anatase. The electrodes were characterized using SEM, EDX, FIB, RAMAN spectroscopy and XRD.

2.2. Coatings

Electrochemical studies were carried out in a three-electrode configuration with the phosphate-doped titania nanotube (pTNT) substrate as working electrode (area of exposure of 0.79 cm^2), Pt foil as counter electrode (1.5 cm^2) and a Ag/AgCI (E^0 = 197 mV_{SHE}) reference electrode (RE). The distance between working and counter electrode was 2 cm. The cyclic voltammetry measurements have been carried out with a potential advance speed of 10 mV/s. The following coating/filling experiments were carried out with annealed samples obtained by 1.5 h anodization in ethylene glycol containing 10 vol% double distilled water, 0.12 M NH_4F and 10 mM $(NH_4)NaH(PO_4)\cdot 4H_2O$.

Selenium was deposited by applying cathodic pulses of −0.4 V vs. RE (1000 pulses, 1 pulse/s, 1 s down time) in an electrolyte containing 2.5 mM Na_2SeO_3, pH 2, adjusted with nitric acid. Silver selenide was deposited from an aqueous solution containing 0.5 M NaSCN, 5 mM $AgNO_3$ and 2.5 mM Na_2SeO_3, pH 2 by applying pulses of −0.5 V (500 pulses, 1 pulse/s, 1 s down time). Copper selenide was deposited from an aqueous solution containing 0.5 M $Cu(CO_2CH_3)_2\cdot H_2O$ and 2.5 mM Na_2SeO_3, pH 1 by applying pulses of −0.5 V (500 pulses, 1 pulse/s, 1 s down time).

HAp was formed by electrochemically assisted precipitation from an electrolyte containing 2.5 mM $Ca(NO_3)_2\cdot 4H_2O$ and 1.5 mM $(NH_4)NaH(PO_4)\cdot 4H_2O$ with and without addition of 2.5 mM Na_2SeO_3, at bath temperatures of 50 ℃ and 60 ℃. The pH value of 3 was adjusted with nitric acid and ammonia. Cathodic polarization was carried out at −5 V for 15 min in a two-electrode configuration to rapidly increase pH at the sample surface and to trigger precipitation of hydroxyapatite. The specimens were cleaned with deionized water and dried with pure ethanol for surface analysis (SEM, XRD).

2.3. Preliminary in vitro experiments

Preliminary *in vitro* experiments were performed with bacteria *Staphylococcus epidermidis*, which colonize the human skin and mucus membranes. Even though its pathogenic potential is relatively low in human hosts, it is one of the main causes of infections in medical implants [20]. This bacteria stem is the most frequent cause of nosocomial infections due to its resistance against penicillin and methicillin. *Staphylococcus epidermidis* ensures its survival by maintaining a balance of commensalism and low virulence instead of aggressively attacking the host. The interaction of biofilm formation and highly different subpopulations causing heterogenic gene expression complicates and dampers possible counter measures [21]. Infections at the biomaterial to bone interface are often involving *Staphylococcus epidermidis* [22] and medical treatment is further impeded by its growing resistance against vancomycin, an alternative antibiotic against multi drug

resistant Staphylococcus [23]. Hence, alternatives to antibiotics have been tested on their ability to inhibit biofilm formation by *Staphylococcus epidermidis* in this work.

In the present studies, the biofilm was formed by overnight cultures of the bacterial isolates grown on Columbia agar plates. Bacteria suspension was adjusted to a McFarland 0.5 (average density of 1×10^6 cells/µL) in 0.9% NaCl solution and diluted to 1:100 in Mueller–Hinton broth. In each well of a 24-well cell culture plate was 1 mL of bacteria dilution filled and one modified Ti-discs placed. The bacteria were incubated for 24 hours at 35 ℃ in ambient air. After incubation, discs were gently washed in PBS (3 mL, three times), followed by rinsing with methanol (95%) for 10 min to immobilize the bacteria cells and a final washing step with distilled water.

3. Results and discussion

3.1. Titania nanotubes

3.1.1. Aqueous phosphate electrolytes

Figure 2a–c shows the dependence of pTNT surface morphology on pH in aqueous phosphate electrolyte. The acidity and the anodization voltage mediate the development of the nanostructure due to competing TiO_2 formation and dissolution reactions [24]. While dissociation of water provides oxygen species for the oxide film growth, fluoride reacts with TiO_2 to the water soluble $[TiF6]^{2-}$ complex, leading to the formation of pits, disturbing and preventing the formation of a passivating TiO_2 layer. Localized pH gradients within the pores with higher acidity at the bottom than at the pore mouth lead finally to the self-assembled nanotubular topography. The formation of $[TiF6]^{2-}$ is essential for the nanotube growth and depends on the pH of the electrolyte ($TiO_2 + 6F^- + 4H^+ \rightarrow [TiF6]^{2-} + 2H_2O$). Whereas, increasing acidity suppresses the hydrolysis ($2H_2O \rightarrow O_2 + 4H^+ + 4e^-$) is required in the formation of TiO_2, and promotes chemical dissolution of TiO_2 according to [25]. Hence, no nanostructure was formed at pH values below 2.

Whereas, at pH 2 (Figure 2a) and 3.3 (Figure 2b), nanotubes were formed with irregular elongated shapes due to fast diffusion and oxidation in the aqueous media interfere. The lack of uniform circular shape is related to fast growth of TiO_2-nanotubes, enabled by the high conductivity of the electrolyte and the relatively high voltage. Moreover, another disrupting influence in aqueous solutions is the recrystallization of dissolved amorphous titania nanotubes as anatase, causing structural changes [8]. At pH 4.7, no nanotopography was evident (Figure 2c) caused by the dominance of the oxide growth over the etching rate due to low acidity.

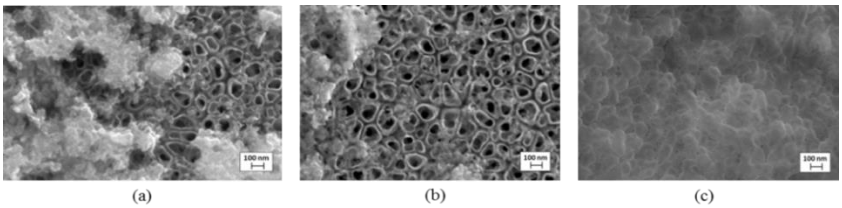

Figure 2. SEM images depicting pH dependence of pTNT growth in aqueous phosphate electrolyte at 20 V: (a) pH 2, (b) pH 3.3, and (c) pH 4.7.

The influence of the anodization voltage is depicted in Figure 3a–c. 10 V led to the growth of pores with a diameter of a few nanometers (Figure 3a), while no nanostructure was obtained at 30 V (Figure 3c) owing to faster potential driven oxide formation than field assisted and chemical dissolution.

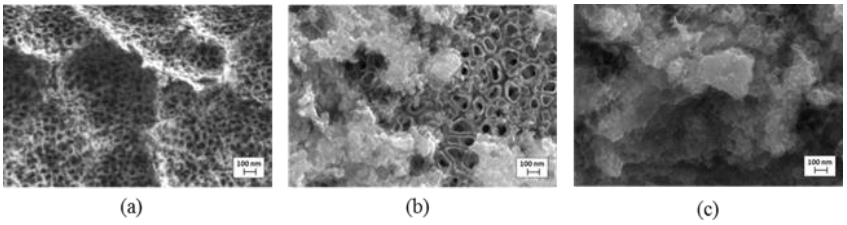

Figure 3. SEM images depicting pH dependence of pTNT growth in aqueous phosphate electrolyte at influence of anodization potential (pH 2, 45 min): (a) 10 V, (b) 20 V, and (c) 30 V.

3.1.2. Ethylene glycol-based electrolytes

In contrast to the aqueous electrolytes, ethylene glycol based electrolytes have high viscosity, limiting the diffusion of fluoride ions and leading to well self-organized nanostructure [5]. However, the water-free ethylene glycol electrolytes have the disadvantage of precipitation of insoluble $[TiF_6]^{2-}$ complex (water-soluble) in the electrolyte during the anodization. Addition of water decreases the viscosity of the electrolyte, increases diffusivity and reduces current densities. The diffusion-controlled process during the anodization improves the balance of dissolution and oxidation [8,26].

Figure 4a–c shows the influence of water content on the nanotubes' diameter at a constant anodization voltage of 20 V. For any metal oxide formation, interaction of the metal with O^{2-} or OH^{-} ions is essential. Compared to anodization in aqueous solution, the availability of any oxygen species in ethylene glycol based electrolyte oxide is more restricted. In absence of water, the native oxide film or oxygen from the atmosphere are the only oxygen sources. Addition of water accelerates the oxide dissolution by increase of H^{+} in the solution and facilitates the formation of $[TiF_6]^{2-}$ [5].

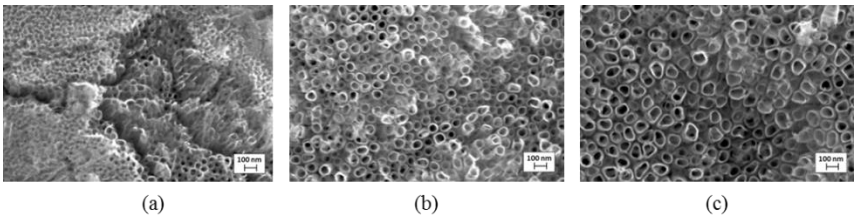

Figure 4. SEM images showing influence of water content on TNT morphology in ethylene glycol based electrolyte: (a) 2 vol%, (b) 10 vol%, and (c) 20 vol%.

Low water percentage of 2 vol% led to nanopores with a diameter of about 40 nm (Figure 4a), while 10 vol% water promoted the growth of separate nanotubes with 60 nm diameter (Figure 4b).

At 20 vol% water, the diameters of the nanotubes were within the 70–130 nm range and differed from the circular shape (Figure 4c) due to the growing influence of water content effecting viscosity and diffusion.

The parameters of 20 V and 10 vol% water led to a well-organized nanotube structure (Figure 5a). While keeping the previous water content (10 vol%), nanotubes' diameters increased to 70 nm upon applying 30 V (Figure 5b). At 40 V the diameters were within the 100–135 nm range (Figure 5c). Obviously, nanotubes' diameters are growing with rising electric field due to subjection to accelerated field assisted dissolution.

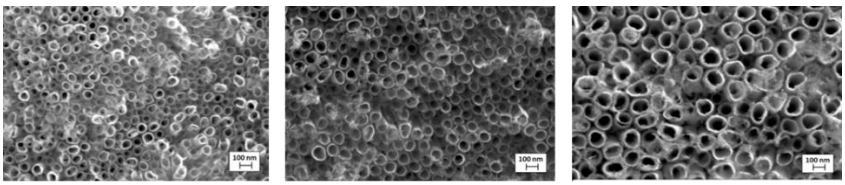

Figure 5. SEM images, effect of anodization potential (10 vol% H_2O, 1.5 h): (a) 20 V, (b) 30 V, and (c) 40 V.

Aiming at incorporation of phosphate and formation of pTNT, $(NH_4)NaH(PO_4)\cdot 4H_2O$ was added to the electrolyte. The following experiments were performed with substrates anodized in ethylene glycol electrolyte containing 10 mM $(NH_4)NaH(PO_4)\cdot 4H_2O$ and 10 vol% water at a constant voltage of 30 V. The tolerated phosphate amount strongly depends on the water content. Nanotube shape and diameter of 100 nm were obtained in an electrolyte containing 10 mM phosphate and 10 vol% water (Figure 6a). EDX analysis confirmed 0.4 wt% P in the layer, which can be correlated to phosphate incorporation [27]. The same amount of P was detected in samples obtained in aqueous phosphate electrolytes as well. Further increase of the phosphate amount in the organic electrolyte to 15 mM (Figure 6b) and of the water content to 20 vol% (Figure 6c) leads to deterioration of the self-ordered nanostructure.

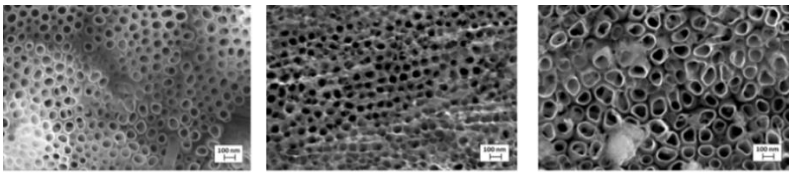

Figure 6. SEM images, effect of phosphate addition in dependence of water content: (a) 10 vol% H_2O, 10 mM $(NH_4)NaH(PO_4)\cdot 4H_2O$; (b) 10 vol% H_2O, 15 mM $(NH_4)NaH(PO_4)\cdot 4H_2O$; (c) 20 vol% H_2O, 15 mM $(NH_4)NaH(PO_4)\cdot 4H_2O$.

3.2. Annealing

Most earlier researchers report that the TiO_2-nanotube layer after anodization is amorphous and do not further specify its nature [8,28]. Annealing of the nanotube array is commonly performed to transform amorphous TiO_2-phase to anatase resulting in improved mechanical properties of the layer.

Furthermore, the TiO_2-anatase accelerates the nucleation of apatite due to lower ζ-potential compared to TiO_2-rutile [29].

XRD measurements were insufficient to identify the TiO_2 species due to detection limit and amorphous phase. Hence, Raman spectroscopy was utilized. The bands of both anatase and rutile phase modifications for samples before heat treatment were identified, although the Raman pattern was affected by noise due to the nanostructure, defected lattice and fluorescence (Figure 7a). Therefore, the spectrum was smoothened using the software Peakfit 4.12 s with a fitting correlation factor r^2 of 97.66%. The main anatase peak at 144 cm^{-1} shifted to 156 cm^{-1} caused by amorphous portion and oxygen deficiency. Annealing led to a blueshift of 12 cm^{-1} overlapping with the anatase reference peak at 144 cm^{-1} due to crystallization of anatase and oxygen uptake from air. The wide broadening of the anatase peak at 198 cm^{-1} was caused by the overlap with the rutile band at 234 cm^{-1}. The wave band at 420 cm^{-1} resulted from the overlap of the characteristic anatase band at 394 cm^{-1} and the rutile peak at 446 cm^{-1}. Whereas, the Raman peak at 514 cm^{-1} showed unambiguously anatase and the wave band at 609 cm^{-1} could be assigned to rutile.

According to Su et al.'s XRD study, the anatase portion of anodic TiO_2 films increases with water content, NH_4F concentration and applied voltage, but no anatase was detected at 30 V [30]. In the current work, Raman spectroscopy revealed that samples, anodized at 30 V in this specific electrolyte composition, contain a mixture of anatase and rutile. The observation confirms the fluoride induced rutile formation found by Kunze et al. who anodized Ti in aqueous phosphorous electrolyte, which comprised no anatase but only amorphous and rutile phase [31]. The presence and ratio of anatase to rutile appears to be dependent on multiple anodization parameters including electrolyte composition and applied voltage. In order to fully understand the conditions and mechanism of the phase formations further experiments need to be conducted.

Subsequent annealing in air (450 ℃, 2 h) apparently transformed rutile to anatase phase (Figure 7b). Selective vertical growth of the TiO_2-nanotubes (indicated by SEM observations) was related to compensation of oxygen deficiency through oxygen consumption from the atmosphere and dehydration of titaniumhydroxide.

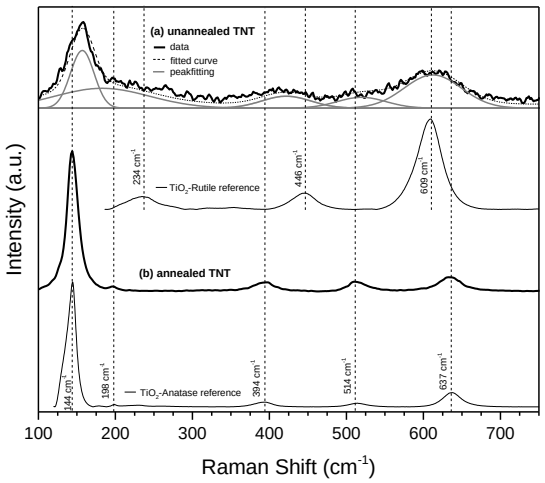

Figure 7. Raman spectroscopy of TNT before (a) and after (b) annealing in air at 450 ℃, including reference data [32].

3.3. Voltammetric studies and deposition of coatings

3.3.1. Selenium

Figure 8 presents voltamogramms for pTNT, Se and Ag_2Se deposition. After immersion of the Ti electrode in nitric acid solution at pH 2 (blank electrolyte), the surface is in passive state. Cathodic reduction of Ti^{4+} to Ti^{3+}, according to the Eq 1:

$$TiOH^{3+} + H^+ + e^- \rightarrow Ti^{3+} + H_2O \quad (1)$$

takes place at a potential of about −0.252 V [33]. A very low current is seen at re-scaling of the voltammogram (not shown). It could be suggested that the reduction process occurs at the bottom of the nanotubes, enhancing the conductivity of the layer. At more negative potentials, the rate of the cathodic reaction strongly increases due to reduction of TiO_2 (Eq 2, $E^0 = -0.699$ V):

$$TiO_2 + 4H^+ + 2e^- \rightarrow Ti^{2+} + 2H_2O \quad (2)$$

and the accompanying hydrogen evolution reaction at potentials more negative than −0.750 mV [34].

In the presence of Se in the electrolyte (added as Na_2SeO_3), a maximum at about −0.4 V was recorded and referred to bulk deposition of Se (Figure 8). The wave from −0.5 to −0.6 V could be associated with the hydrogen selenide formation according to the Eqs 3–4 [35]:

$$Se^0 + 2H^+ + 2e^- \rightarrow H_2Se \quad (3)$$

$$H_2SeO_3 + 6e^- + 6H^+ \rightarrow H_2Se + 3H_2O \quad (4)$$

The formation of selenide leads to the coupled chemical reduction and Se formation (Eq 5):

$$H_2SeO_3 + 2H_2Se \rightarrow 3Se^0 + 3H_2O \quad (5)$$

Accumulation of amorphous Se on the electrode surface is the probable reason for the hindering of the overall cathodic reaction.

Deposition experiments by constant polarization at −0.4 V produced a dense layer of Se on top of the nanotubes. Change in the color of the coating with increasing deposition time from a bright red to a reddish dark grey was observed.

A pulse function was applied to incorporate Se into the nanotubes. The as-deposited Se is amorphous and gave no XRD signals. The surface morphology of the layer is shown in Figure 9a, containing about 11 wt% Se according to EDX analysis. The FIB cross-section (Figure 9b) showed uniformly Se filled nanotubes with up to 11 wt% Se (top-section 11.3 wt%, mid-section 10.9 wt%, bottom-section 7.1 wt%, values detected by EDX).

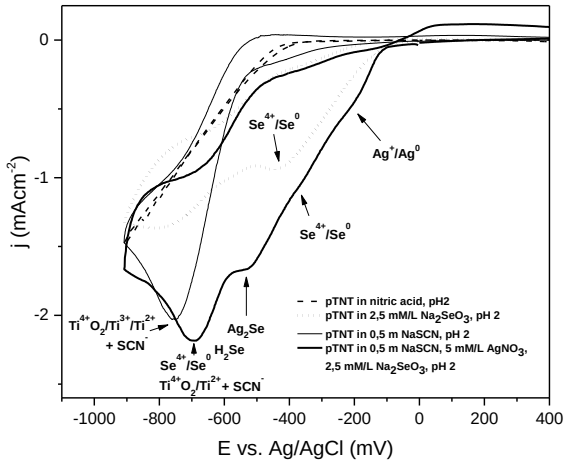

Figure 8. Voltammograms of pTNT, Se and Ag_2Se deposition.

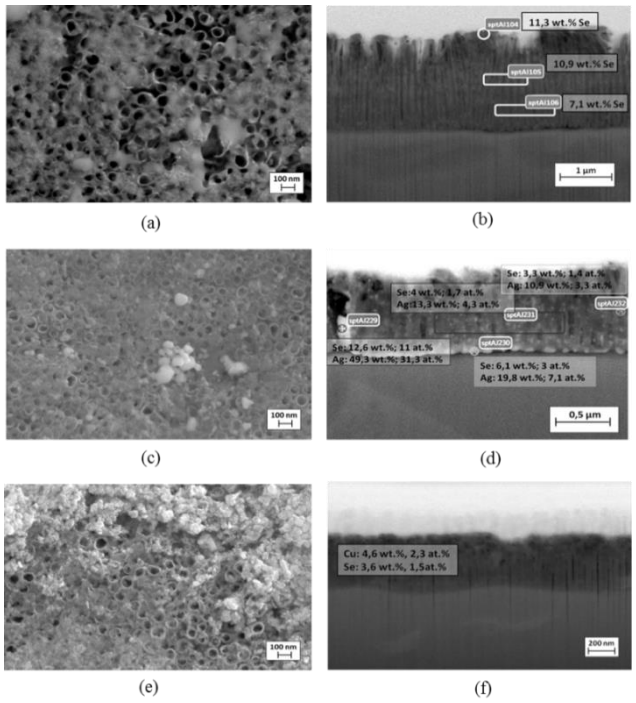

Figure 9. SEM images of (a) Se–pTNT, (c) Ag_2Se–pTNT, (e) Cu_2Se–pTNT and cross-sections (FIB-SEM) of (b) Se–pTNT, (d) Ag_2Se–pTNT, (f) Cu_2Se–pTNT.

3.3.2. Silver selenide and copper selenide

In order to achieve proximity in the deposition potentials of Ag and Se and for alloy formation, thiocyanate was used as complexing agent for Ag.

Figure 8 presents a voltammogram for pTNT in the blank solution containing thiocyanate (thin solid line). An increase in the rate of the cathodic reaction in both potential ranges related to reduction of Ti^{4+} to Ti^{3+} (Eq 1) and to Ti^{2+} (Eq 2) is observed and associated with complex formation of the reduced species with thiocyanate. The suppression of the cathodic reaction is probably due to

diffusion limitation for thiocyanate to the electrode surface as well as of reaction products (Ti-thiocyanate complexes) from the electrode surface to the electrolyte bulk. Addition of thiocyanate to the electrolyte containing Ag and Se polarizes the Ag^+ reduction reaction to a potential of about −0.25 V and a polarization wave is recorded (Figure 8, thick solid line). At a more negative potential of about −0.4 V bulk deposition of Se takes place. Separate voltammetric experiments showed no effect of the thiocyanate on the Se deposition. Silver selenide was formed at a potential of about −0.5 V (Eqs 6–7) [36]:

$$2Ag(SCN)_n^{1-n} + Se + 2e^- \rightarrow Ag_2Se + 2nSCN^- \quad (6)$$

$$2Ag(SCN)_n^{1-n} + HSeO_3^- + 6e^- \rightarrow Ag_2Se + 3H_2O + 2nSCN^- \quad (7)$$

At potentials of about −0.7 V the formation of H_2Se, Se and reduction of Ti^{4+} to Ti^{2+} overlapped. The Ag_2Se alloy deposition was performed on pTNT by applying pulses of −0.5 V. Top view of the surface is presented in Figure 9c. Analyses in the cross-section area show concentration gradient for Ag in depth (Figure 9d). The deposition process of copper selenide was investigated in a similar manner by voltammetry. A potential of at about −0.5 V was chosen for the co-deposition of Cu and Se in agreement with literature data [37]. Top view of the sample surface after pulse deposition at −0.5 V is presented in Figure 9e. Particles agglomeration and partial coverage of the nanotubes' openings were observed. EDX measurements in the cross-section area confirmed Cu and Se in amounts of 4.6 wt% and 3.6 wt%, respectively (Figure 9f).

3.3.3. Hydroxyapatite

The HAp coating's quality of adhesion is dependent on the substrate's surface structure, the bath's acidity, the applied voltage and bath temperature [38]. To prevent precipitation of HAp in the solution, the pH has to be in an acidic range (pH < 4). Applying cathodic polarization causes a vigorous hydrogen evolution at the bottom of the nanotubes leading to HAp crystal formation (Eq 8), acting as an anchorage for the growing layer.

$$10Ca^{2+} + 6PO_4^{2-} + 2OH^- \rightarrow Ca_{10}(PO_4)_6(OH)_2 \quad (8)$$

The template effect of the nanostructure on the HAp formation was followed by using Ti samples with different topography. On a pure Ti sample, grinded and polished gradually with P180, P360, P500, P1200, P2000, P4000, crystals grew fibrously parallel to the substrate surface indicating poor layer adhesion (Figure 10a). Whereas a more compact HAp coating was formed on unannealed pTNT obtained by anodization in aqueous phosphate electrolyte (Figure 10b). HAp adhesion was improved by addition of Se and use of annealed TNT substrate, obtained by anodization in ethylene glycol electrolyte (Figure 10c). The HAp crystal growth was facilitated by the presence of anatase [29].

Formation of HAp needles was induced by raising the bath temperature from 50 to 60 ℃ (Figure 10d–e). Furthermore, aiming at incorporation of Se in the HAp layer, Na_2SeO_3 was added to the solution. It could be proposed that at the conditions of the experiment, Se^{4+} reduction and formation of Se takes place, influencing the HAp nucleation behavior by suppressing the hydrogen evolution reaction. Furthermore, formation of fine globular crystal bundles on top of the HAp needles was promoted (Figure 10e). According to the literature, HAp with large external surface would provide high resorption, while the crystalline HAp underneath would ensure the mechanical stability of the layer [18].

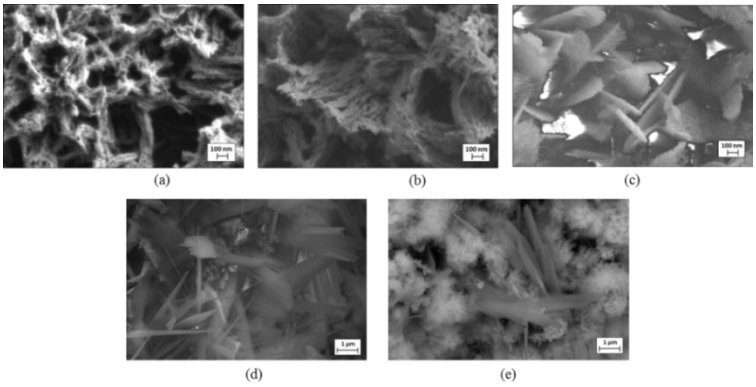

Figure 10. SEM images showing the influence of the substrate topography and bath temperature on HAp deposition for (a) polished Ti, 50 ℃; (b) unannealed pTNT from aqueous phosphate electrolyte, 50 ℃; (c) Se–HAp on unannealed pTNT from ethylene glycol based electrolyte, 50 ℃; (d) annealed pTNT from ethylene glycol electrolyte, 60 ℃; (e) Se–HAp on annealed pTNT from ethylene glycol electrolyte, 60 ℃.

3.4. Phase characterization

XRD analysis of the annealed pTNTs on Ti6Al4V substrates (Figure 11a) showed characteristic pattern of the substrate—hexagonal $Ti_{0.94}V_{0.01}Al_{0.05}$, which indicates that V is dissolved at a higher rate than Al during the anodization process.

Figure 11b confirms the presence of Ag_2Se in the electrochemically deposited layer with a matching pattern of orthorhombic naumannite. The XRD pattern in Figure 11c reveals two compounds of copper selenide: tetragonal Cu_3Se_2 and cubic $Cu_{1.82}Se$ (denoted as Cu_2Se–pTNT). According to Lippkow D. et al., small amounts of excessive codeposited Se and/or Cu causes formation of Cu_3Se_2 as a by-product of Cu_2Se [39]. Exposure of Cu_2Se to oxygen also results in mixed valent copper (Cu^+, Cu^{2+}) [40]. The recorded pattern in Figure 11d could be ascribed to pure hydroxyapatite [41]. Se is not detected by XRD because of presence in an amorphous state.

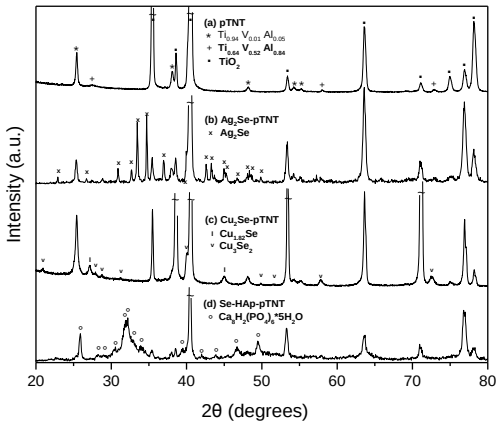

Figure 11. XRD patterns of (a) pTNT, (b) Ag_2Se–pTNT, (c) Cu_2Se–pTNT, and (d) Se–HAp–pTNT.

3.5. In vitro experiments

The biofilm was investigated via SEM in order to determine applied coatings' ability to prevent the biofilm formation. The immobilized bacteria cells have a round shape and a diameter of approximately 1 µm. Figure 12a shows bacteria cells on the polished substrate Ti6Al4V forming colonies of dozens of cells. Whereas, titania nanotubes with a diameter of 70 nm enabled the formation of a thick biofilm (Figure 12b) by highly increasing the surface area. In contrast to TNT, alteration of the anodization parameters lead to nanotubes of 100 nm (pTNT, Figure 12c), which reduces the amount of attached bacteria and size of colonies and correlates with literature about the influence of nanotube diameter on Staphylococcus aureus and epidermidis [6, 10, 11]. The deposition of elementary selenium increases the protection against bacterial adhesion significantly (Figure 12d), so that only isolated bacteria cells are located. The hydroxyapatite deposited pTNT (Figure 12e) is rough and offers plenty of edges for bacteria to harbor. The amount and size of bacteria colonies is comparable with the polished substrate (Figure 12a). Whereas, no bacteria cells have been found on the SeHAp–pTNT.

To demonstrate the difference between silver selenide and silver in the layer, a silver coated nanostructured Ti-disc was prepared with nanoscale silver trapped in the nanopores (4.5 wt% Ag). Figure 12g shows Ag–pTNT covered by a slightly thinner biofilm compared to TNT (Figure 12b), which is a result of S. epidermidis' capability to reduce silver nanoparticles' toxicity by precipitating nanocristalline silver in its cytoplasma [42]. In contrast to Ag–pTNT, the biggest groups of bacteria cells on Ag_2Se–pTNT (Figure 12h) consists of up to three cells and is situated in areas where less silver selenide coverage is present. Figure 12i presents Cu_2Se–pTNT's antibacterial activity resulting in isolated or at most groups of two cells with relatively big distances in between.

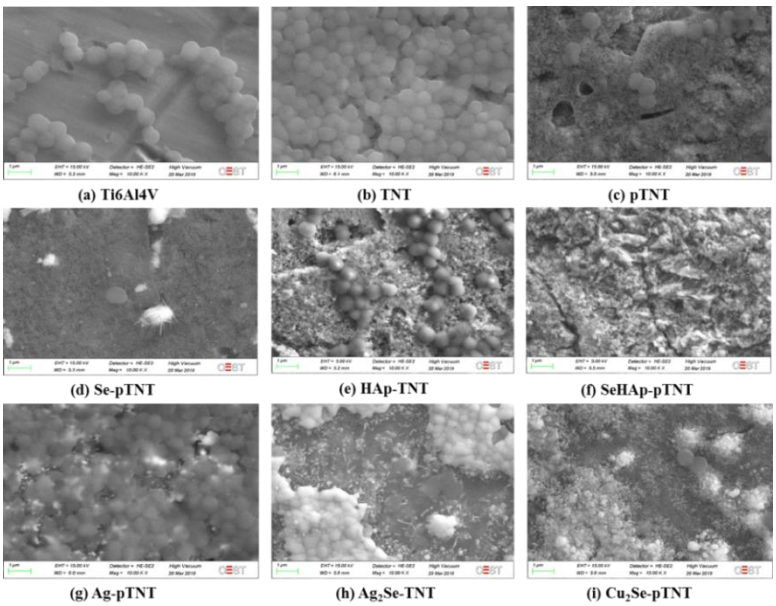

Figure 12. SEM images of immobilized bacteria after 24 h incubation.

4. Conclusions

In this study, various strategies were combined to modify Ti- based material, aiming at enhanced antibacterial properties and biocompatibility.

Nano-topography formation by anodization was studied. Uniform nano-tube-shaped structures with a diameter of 100 nm, containing phosphate were successfully grown on Ti and Ti6Al4V alloy. As-prepared samples were uniformly filled with Se, Ag_2Se and Cu_2Se.

Hydroxyapatite was electro-chemically deposited on the pTNT. It was found that addition of Se to the electrolyte influences the HAp nucleation. The formation of fine globular crystal bundles on top of the HAp needles approximates a two- phase coating, expected to provide high resorption, bioactivity as well as mechanical stability.

In vitro studies show effective hindering of biofilm formation by applying Se, Se- compounds surface modification with Se–pTNT and Cu_2Se–pTNT performing best.

Such samples will be further examined in depth in medical in-vitro and in-vivo experiments and undergo clinical tests to evaluate its feasibility for biomedical application.

Acknowledgements

These investigations were performed with the support of the Austrian Science Foundation FFG under Grant 4253627.

Conflict of interests

All authors declare no conflicts of interest in this paper.

References

1. Technavio Research, Biomedical metal market-global forecasts and opportunity, 2018 Available from: https://www.businesswire.com/news/home/20170620006368/en/Biomedical-Metal-Market---Global-Forecasts-Opportunity.
2. Actis L, Gaviria L, Guda T, et al. (2013) Antimicrobial surfaces for craniofacial implants: state of the art. *J Korean Assoc Oral Maxillofac Surg* 39: 43–54.
3. Chatzopoulos GS, Wolff LF (2017) Implant failure and history of failed endodontic treatment: a retrospective case-control study. *J Clin Exp Dent* 9: e1322–e1328.
4. Darouiche RO (2004) Treatment of infections associated with surgical implants. *N Engl J Med* 350: 1422–1429.
5. Naghizadeh M, Ghannadi S, Abdizadeh H, et al. (2014) Effect of fluoride concentration and water content on morphology of titania nanotubes in ethylene glycol solution. *Adv Mater Res* 829: 907–911.
6. Xu Z, Lai Y, Wu D, et al. (2015) Increased mesenchymal stem cell response and decreased staphylococcus aureus adhesion on titania nanotubes without pharmaceuticals. *Biomed Res Int* 2015: 9.

7. Jagminas A, Kovger J, Selskis A, et al. (2015) Effect of hydrogen doping on the loading of titania nanotube films with copper selenide species via alternating current deposition. *J Appl Electrochem* 45: 1141–1151.
8. Cao C, Yan J, Zhang Y, et al. (2016) Stability of titania nanotube arrays in aqueous environment and the related factors. *Sci Rep* 6: 23065.
9. Lim YC, Siti AS, Amiera PN, et al. (2017) Electrochemical deposition of copper decorated titania nanotubes and its visible light photocatalytic performance. *AIP Conf Proc* 1877: 070002.
10. Ercan B, Taylor E, Alpaslan E, et al. (2011) Diameter of titanium nanotubes influences anti-bacterial efficacy. *Nanotechnology* 22: 295102.
11. Su EP, Justin DF, Pratt CR, et al. (2018) Effects of titanium nanotubes on the osseointegration, cell differentiation, mineralisation and antibacterial properties of orthopaedic implant surfaces. *Bone Joint J* 100-B: 9–16.
12. Piszczek P, Lewandowska Ż, Radtke A, et al. (2017) Biocompatibility of titania nanotube coatings enriched with silver nanograins by chemical vapor deposition. *Nanomaterials* 7: 274.
13. Holinka J, Pilz M, Kubista B, et al. (2013) Effects of selenium coating of orthopaedic implant surfaces on bacterial adherence and osteoblastic cell growth. *Bone Joint J* 95-B: 678–682.
14. Liu W, Golshan NH, Deng X, et al. (2016) Selenium nanoparticles incorporated into titania nanotubes inhibit bacterial growth and macrophage proliferation. *Nanoscale* 8: 15783–15794.
15. Mir IA, Alam H, Priyadarshini E, et al. (2018) Antimicrobial and biocompatibility of highly fluorescent znse core and znse@zns core-shell quantum dots. *J Nanopart Res* 20: 174.
16. Capanema N, Mansur A, Carvalho S, et al. (2015) Niobium-doped hydroxyapatite bioceramics: synthesis, characterization and in vitro cytocompatibility. *Materials* 8: 4191–4209.
17. Bang LT, Long BD, Othman R (2014) Carbonate hydroxyapatite and silicon-substituted carbonate hydroxyapatite: synthesis, mechanical properties, and solubility evaluations. *Sci World J* 2014: 969876.
18. Xue W, Liu X, Zheng X, et al. (2005) Effect of hydroxyapatite coating crystallinity on dissolution and osseointegration *in vivo*. *J Biomed Mater Res A* 74: 553–561.
19. Bauer S, Kleber S, Schmuki P (2006) TiO_2 nanotubes: tailoring the geometry in H_3PO_4/HF electrolytes. *Electrochem Commun* 8: 1321–1325.
20. Rogers KL, Fey PD, Rupp ME (2009) Coagulase-negative staphylococcal infections. *Infect Dis Clin N Am* 23: 73–98.
21. Schoenfelder SMK, Lange C, Eckart M, et al. (2010) Success through diversity—how staphylococcus epidermidis establishes as a nosocomial pathogen. *Int J Med Microbiol* 300: 380–386.
22. Tammelin A, Domicel P, Hambraeus A, et al. (2000) Dispersal of methicillin-resistant staphylococcus epidermidis by staff in an operating suite for thoracic and cardiovascular surgery: relation to skin carriage and clothing. *J Hosp Infect* 44: 119–126.
23. Issam R, Amin A, Kenneth R (1998) Staphylococcus epidermidis: emerging resistance and need for alternative agents. *Clin Infect Dis* 26: 1182–1187.

24. Beranek R, Hildebrand H, Schmuki P (2003) Self-organized porous titanium oxide prepared in H_2SO_4/HF electrolytes. *Electrochem Solid St* 6: B12–B14.
25. Schmidt J, Vogelsberger W (2006) Dissolution kinetics of titanium dioxide nanoparticles: The observation of an unusual kinetic size effect. *J Phys Chem* 110: 3955–3963.
26. Berger S, Kunze J, Schmuki P, et al. (2010) Influence of water content on the growth of anodic TiO_2 nanotubes in fluoride-containing ethylene glycol electrolytes. *J Electrochem Soc* 157: C18–C23.
27. Ghicov A, Tsuchiya H, Macak JM, et al. (2005) Titanium oxide nanotubes prepared in phosphate electrolytes. *Electrochem Commun* 7: 505–509.
28. Albu, SP, Ghicov A, Aldabergenova S, et al. (2008) Formation of double-walled TiO_2 nanotubes and robust anatase membranes. *Adv Mater* 20: 4135–4139.
29. Svetina M, Ciacchi LC, Sbaizero O, et al. (2001) Deposition of calcium ions on rutile (110): a first-principles investigation. *Acta Mater* 49: 2169–2177.
30. Su Z, Zhang L, Jiang F, et al. (2013) Formation of crystalline TiO_2 by anodic oxidation of titanium. *Prog Nat Sci* 23: 294–301.
31. Kunze J, Seyeux A, Schmuki P (2008) Anodic TiO_2 layer conversion: fluoride-induced rutile formation at room temperature. *Electrochem Solid State* 11: K11–K13.
32. Lafuente B, Downs RT, Yang H, et al. (2015) The power of databases: the rruff project, In: Armbruster T, Danisi RM, *Highlights in Mineralogical Crystallography*, Germany: Walter de Gruyter GmbH, 1–29.
33. Haynes WM (2011) *CRC Handbook of Chemistry and Physics*, 92th edition, CRC Press: Boca Raton 5–84.
34. Khalil MW, Abdel Rahim MA (1991) Hydrogen evolution reaction on titanium and oxide-covered titanium electrodes. *Materialwiss Werkst* 22: 390–395.
35. Saji VS, Lee CW (2013) Selenium electrochemistry. *RSC Adv* 3: 10058–10077.
36. David M， Modolo R， Traore M， et al. (1986) Cheminform abstract: Electrodeposition and electrodissolution of semiconductor-metal mixed compounds. Part 1. Silver selenide. *Chem Inform* 17.
37. Moysiadou A, Koutsikou R, Bouroushian M (2015) Pulse electrodeposition of copper selenides from acidic aqueous baths. *Mater Lett* 139: 112–115.
38. Parcharoen Y, Termsuksawad P, Sirivisoot S (2016) Improved bonding strength of hydroxyapatite on titanium dioxide nanotube arrays following alkaline pretreatment for orthopedic implants. *J Nanomater* 2016: 9143969.
39. Lippkow D, Strehblow HH (1998) Structural investigations of thin films of copper-selenide electrodeposited at elevated temperatures. *Electrochim Acta* 43: 2131–2140.
40. Riha SC, Johnson DC, Prieto AL (2011) Cu_2Se nanoparticles with tunable electronic properties due to a controlled solid-state phase transition driven by copper oxidation and cationic conduction. *J Am Chem Soc* 133: 1383–1390.
41. Rezakhani A, Kashani Motlagh MM (2012) Synthesis and characterization of hydroxyapatite nanocrystal and gelatin doped with Zn^{2+} and cross linked by glutaraldehyde. *Int J Phys Sci* 7: 2768–2774.

42. Rezvani Amin Z, Khashyarmanesh Z, Fazly Bazzaz BS (2016) Different behavior of staphylococcus epidermidis in intracellular biosynthesis of silver and cadmium sulfide nanoparticles: more stability and lower toxicity of extracted nanoparticles. *World J Microb Biot* 32: 140.